Nonlinear coupling between axisymmetrically-polarized ultrashort optical pulses in a uniaxial crystal

Masato Suzuki,[1] **Keisaku Yamane,**[1,2] **Kazuhiko Oka,**[1] **Yasunori Toda,**[1,2] **and Ryuji Morita**[1,2,*]

[1]*Department of Applied Physics, Hokkaido University, Kita-13, Nishi-8, Kita-ku, Sapporo 060-8628, Japan*

[2]*JST, CREST, Kita-13, Nishi-8, Kita-ku, Sapporo 060-8628, Japan*

[*]*morita@eng.hokudai.ac.jp*

http://iphys3-ap.eng.hokudai.ac.jp/english/index.html

Abstract: Nonlinear propagation of focused axisymmetrically-polarized ultrashort optical pulses along the optic axis in a uniaxial crystal is investigated experimentally and theoretically. The energy transfer between an azimuthally-polarized pulse and a radially-polarized pulse is observed. To analyze the nonlinear propagation, a general paraxial equation with a third-order nonlinearity for axisymmetrically-polarized pulses in a uniaxial crystal is derived and the extended Stokes parameters (ESPs) based on cylindrical coordinates are newly-introduced. The simulation results by using this equation, providing the calculated ESPs, well explain our experimental observations: 1) the energy transfer is attributed to the four-wave-mixing effect, reflecting the overlapping between the axisymmetrically polarized modes, 2) the variations of the polarization defined from the ESPs are clarified to be affected by the self- and the cross-phase modulations, which make the effective propagation length long or short.

OCIS codes: (050.4865) Optical vortices; (190.4380) Nonlinear optics, four-wave mixing; (190.3270) Kerr effect.

References and links

1. C. Hnatovsky, V, Shvedov, W, Krolikowski, and A, Rode, "Revealing local field structure of focused ultrashort pulses," Phys. Rev. Lett. **106**, 123901 (2011).
2. J. Hamazaki, R. Morita, K. Chujo, Y. Kobayashi, S. Tanda, and T. Omatsu, "Optical-vortex laser ablation," Opt. Express **18**, 2144–2151 (2010).
3. T. Omatsu, K. Chujo, K. Miyamoto, M. Okida, K. Nakamura, N. Aoki, and R. Morita, "Metal microneedle fabrication using twisted light with spin," Opt. Express **18**, 17967–17973 (2010).
4. K. Toyoda, K. Miyamoto, N. Aoki, R. Morita, and T. Omatsu, "Using optical vortex to control the chirality of twisted metal nanostructures," Nano Lett. **12**, 3645–3649 (2012).
5. N. M. Litchinitser, "Structured light meets structured matter," Science **337**, 1054–1055 (2012).
6. K. Toyoda, F. Takahashi, S. Takizawa, Y. Tokizane, K. Miyamoto, R. Morita, and T. Omatsu, "Transfer of light helicity in nanostructures," Phys. Rev. Lett. **110**, 143603 (2013).
7. Y. Tokizane, K. Shimatake, Y. Toda, K. Oka, M. Tsubota, S. Tanda, and R. Morita, "Global evaluation of closed-loop electron dynamics in quasi-one-dimensional conductors using polarization vortices," Opt. Express **17**, 24198–24207 (2009).
8. L. Novotny, M. R. Beversluis, K. S. Youngworth, and T. G. Brown, "Longitudinal field modes probed by single molecules," Phys. Rev. Lett. **86**, 5251–5254 (2001).

#211988 - $15.00 USD Received 13 May 2014; revised 24 Jun 2014; accepted 24 Jun 2014; published 2 Jul 2014

9. Y. I. Salamin and C. H. Keitel, "Electron acceleration by a tightly focused laser beam," Phys. Rev. Lett. **88**, 095005 (2002).
10. Q. Zhan, "Trapping metallic Rayleigh particles with radial polarization," Opt. Express **12**, 3377–3382 (2004).
11. Y. S. Rumala, G. Milione, T. A. Nguyen, S. Pratavieira, Z. Hossain, D. Nolan, S. Slussarenko, E. Karimi, L. Marrucci, and R. R. Alfano, "Tunable supercontinum light vector vortex beam generator using a q-plate," Opt. Lett. **38**, 5083–5086 (2013).
12. S. Ramachandran, P. Kristensen, and M. F. Yan, "Generation and propagation of radially polarized beams in optical fibers," Opt. Lett. **34**, 2525–2527 (2009).
13. K. S. Youngworth and T. G. Brown, "Focusing of high numerical aperture cylindrical-vector beams," Opt. Express **7**, 77–87 (2000).
14. C. Maurer, A. Jesacher, S. Fürhapter, S. Bernet, and M. Ritsch-Marte, "Tailoring of arbitrary optical vector beams," New J. Phys. **9**, 78 (2007).
15. L. Allen, M. W. Beijersbergen, R. J. C. Spreeuw, and J. P. Woerdman, "Orbital angular momentum of light and the transformation of Laguerre-Gaussian laser modes," Phys. Rev. A **45**, 8185–8189 (1992).
16. Y. Tokizane, K. Oka, and R. Morita, "Supercontinuum optical vortex pulse generation without spatial or topological-charge dispersion," Opt. Express **17**, 14517–14525 (2009).
17. M. Stalder and M. Schadt, "Linearly polarized light with axial symmetry generated by liquid-crystal polarization converters," Opt. Lett. **21**, 1948–1950 (1996).
18. V. G. Shvedov, C. Hnatovsky, W. Krolikowski, and A. V. Rode, "Efficient beam converter for the generation of high-power femtosecond vortices," Opt. Lett. **35**, 2660–2662 (2010).
19. Y. Izdebskaya, E. Brasselet, V. Shvedov, A. Desyatnikov, W. Krolikowski, and Y. Kivshar, "Dynamics of linear polarization conversion in uniaxial crystals," Opt. Express **17**, 18196–18208 (2009).
20. A. Volyar, V. Shvedov, T. Fadeyeva, A. S. Desyatnikov, D. N. Neshev, W. Krolikowski, and Y. S. Kivshar, "Generation of single-charge optical vortices with an uniaxial crystal," Opt. Express **14**, 3724–3729 (2006).
21. T. Fadeyeva, A. Rubass, Y. Egorov, A. Volyar, and G. Swartzlander, Jr., "Quadrefringence of optical vortices in a uniaxial crystal," J. Opt. Soc. Am. A **25**, 1634–1641 (2008).
22. T. A. Fadeyeva and A. V. Volyar, "Extreme spin-orbit coupling in crystal-traveling paraxial beams," J. Opt. Soc. Am. A **27**, 381–389 (2010).
23. V. Shvedov, W. Krolikowski, A. Volyar, D. N. Neshev, A. S. Desyatnikov, and Y. S. Kivshar, "Focusing and correlation properties of white-light optical vortices," Opt. Express **13**, 7393–7398 (2005).
24. G. P. Agrawal, *Nonlinear Fiber Optics*, 2nd ed. (Academic, 1995).
25. C. Shang and H. Hsu, "The spatial symmetric forms of third-order nonlinear susceptibility," IEEE J. Quantum Electron. **23**, 177–179 (1987).
26. G. Milione, H. I. Sztul, D. A. Nolan, and R. R. Alfano, "Higher-order Poincaré sphere, Stokes parameters, and the angular momentum of light," Phys. Rev. Lett. **107**, 053601 (2011).
27. M. R. Dennis, "Polarization singularities in paraxial vector fields: morphology and statistics," Opt. Commun. **213**, 201–221 (2002).
28. E. Brasselet, Y. Izdebskaya, V. Shvedov, A. S. Desyatnikov, W. Krolikowski, and Y. S. Kivshar, "Dynamics of optical spin-orbit coupling in uniaxial crystals," Opt. Lett. **34**, 1021–1023 (2009).
29. L. Marrucci, C. Manzo, and D. Paparo, "Optical spin-to-orbital angular momentum conversion in inhomogeneous anisotropic media," Phys. Rev. Lett. **96**, 163905 (2006).
30. K. Y. Bliokh, E. A. Ostrovskaya, M. A. Alonso, O. G. Rodríguez-Herrera, D. Lara, and C. Dainty, "Spin-to-orbital angular momentum conversion in focusing, scattering, and imaging systems," Opt. Express **19**, 26132–26149 (2011).
31. G. Zhan, K. Oka, T. Ishigaki, and N. Baba, "Birefringent imaging spectrometer," Appl. Opt. **41**, 734–738 (2002).
32. W. J. Tropf and M. E. Thomas, "Properties of Crystals and Glasses," in *Optical Properties of Materials, Nonlinear Optics, Quantum Optics*, Vol. IV of Handbook of Optics, M. Bass, G. Li, and E. V. Stryland, eds. (McGraw-Hill, 2010), Chapter 2.
33. J. Hamazaki, Y. Mineta, K. Oka, and R. Morita, "Direct observation of Gouy phase shift in a propagating optical vortex," Opt. Express **14**, 8382–8392 (2006).
34. A. M. Beckley, T. G. Brown, and M. A. Alonso, "Full Poincaré beams," Opt. Express **18**, 10777–10785 (2010).
35. E. J. Weniger, "On the analyticity of Laguerre series," J. Phys. A: Math. Theor. **41**, 425207 (2008).

1. Introduction

Axisymmetrically-polarized modes, such as a radially-polarized (RP) mode and an azimuthally-polarized (AP) mode, have attracted considerable attention for application to laser processing [1–6], spectroscopy of a ring shaped material [7], super-resolution microscopy [8], particle acceleration [9], laser trapping [10], and telecommunications [11, 12]. They have annular-shaped intensity profile owing to the polarization singularity in the beam center. More-

#211988 - $15.00 USD Received 13 May 2014; revised 24 Jun 2014; accepted 24 Jun 2014; published 2 Jul 2014

over, tightly focused with high numerical aperture (NA) lenses, the radially- and azimuthally-polarized beams have respectively longitudinal electric and magnetic field components around the foci where their spot sizes are beyond the diffraction limit [13].

The axisymmetrically-polarized modes can be decomposed into the left-circularly polarized (LCP), right-handed optical vortex (OV) $|s=+1\rangle|l=-1\rangle$ and the right-circularly polarized (RCP), left-handed OV $|s=-1\rangle|l=+1\rangle$ [14]. Here indices s and l are respectively the spin angular momentum (SAM) and the orbital angular momentum (OAM) of light per photon in $\hbar$ units. The OAM originates in the phase ramp $\exp(\mathrm{i}l\phi)$ (ϕ is azimuthal angle) of OV around the phase singular point [15]. Superpositions of a RP mode and an AP mode express any axisymmetrically polarized modes because the $|s=+1\rangle|l=-1\rangle$ or the $|s=-1\rangle|l=+1\rangle$ OV mode is expressed as a superposition of a RP mode and an AP mode.

The preceding study [1] shows the generation and the separation of a RP pulse and an AP pulse from an $|s=+1\rangle|l=-1\rangle$ ($|s=-1\rangle|l=+1\rangle$) OV pulse with their linear propagation along the optic axis in a uniaxial crystal. The separation is ascribed to the phenomenon that the RP and the AP modes undergo different refractive indices of the crystal and thus have different focal points [1]. Such scheme using a uniaxial crystal is suited for ultrashort axisymmetrically-polarized pulse generation because the bandwidth is broader than those in other method using a photonic-crystal axially-symmetric polarizer/waveplate [16] and a liquid-crystal polarization converters [17]. While [1] and [18–23] investigated only the linear effect by inputting a CW beam or a diverging pulse into a uniaxial crystal, the nonlinear effects such as Kerr and four-wave-mixing (FWM) effects have not been well investigated so far. In particular, the nonlinear effects by axisymmetrically-polarized pulses in the ultrafast regime, which are crucial for applications using them, have not been substantially studied.

In the present paper, we experimentally and theoretically investigate ultrashort pulse propagation in a uniaxial crystal through the nonlinear effects between a RP mode and an AP mode. To analyze the experimental results, we derive a general paraxial equation with a third-order nonlinearity for axisymmetrically-polarized pulses in a uniaxial crystal and newly introduce the extended Stokes parameters (ESPs) based on cylindrical coordinates. Comparing the experimental and the simulation results, we clarify the nonlinear coupling mechanism between axisymmetrically-polarized ultrashort optical pulses in a uniaxial crystal.

The paper is organized as follows. In section 2.1, we first formulate the nonlinear wave equation for the propagation of the axisymmetrically-polarized modes in a uniaxial crystal. To characterize the non-uniform spatial polarization, we also introduce the ESPs based on cylindrical coordinates and the degree of polarization (DOP) in section 2.2. Some preliminary simulations for the linear propagation case are demonstrated in section 2.3. The experimental setup is summarized in section 3.1. The main findings are given in section 3.2, which describe the experimental results. In section 4, in terms of the ESPs and the modified DOP, we address the nonlinear coupling effects between the axisymmetrically-polarized pulses in the crystal. Comparison between the experimental and simulation results is also commented on in section 4. Finally, section 5 summarizes the conclusion.

2. Theoretical formulation

2.1. Wave equation

In order to obtain a wave equation in a uniaxial crystal, we suppose that the electric flux density $\mathbf{D}$ is described as

$$\mathbf{D}(\mathbf{r},t)=\varepsilon\mathbf{E}(\mathbf{r},t)+\mathbf{P}^{\mathrm{NL}}(\mathbf{r},t). \tag{1}$$

Here, ε is the permittivity tensor, where $\varepsilon_{xx}=\varepsilon_{yy}=\varepsilon_{\mathrm{o}}$ (the ordinary permittivity), $\varepsilon_{zz}=\varepsilon_{\mathrm{e}}$ (the extraordinary permittivity) and $\varepsilon_{ij}=0$ ($i\neq j$) [20], $\mathbf{E}$ is the real electric field and $\mathbf{P}^{\mathrm{NL}}$ is the

#211988 - $15.00 USD Received 13 May 2014; revised 24 Jun 2014; accepted 24 Jun 2014; published 2 Jul 2014

real nonlinear polarization. All field variables are functions of position $\mathbf{r} = (x, y, z)$ and time t.

For a many-cycle optical pulse propagating along the optic axis with small beam divergence (NA $\lesssim 0.1$), the real electric field and the real nonlinear polarization can be written as $\mathbf{E}(\mathbf{r},t) = \mathrm{Re}[\tilde{\mathbf{E}}(\mathbf{r})\exp[\mathrm{i}(kz-\omega t)]]$ and $\mathbf{P}^{\mathrm{NL}}(\mathbf{r},t) = \mathrm{Re}[\tilde{\mathbf{P}}^{\mathrm{NL}}(\mathbf{r})\exp[\mathrm{i}(kz-\omega t)]]$, respectively. Here $\tilde{\mathbf{E}}$, $\tilde{\mathbf{P}}^{\mathrm{NL}}$, $k = \omega/c$, ω and c are the complex slowly-varying amplitude vector, the complex slowly-varying nonlinear polarization vector, the propagation constant, the angular frequency and the velocity of light in vacuum, respectively. This approximation works in pulses whose duration is over $\sim$100 fs for a wavelength $\sim$800 nm (where $\omega \sim 10^{15}$ s^{-1}) [24]; in addition, our theoretical model here is applicable to pulses with temporally Gaussian- or hyperbolic-secant-shaped envelopes. We consider the $\chi^{(3)}$ nonlinearity of trigonal ($3m$, $-3m$, 32) and hexagonal (622, $6mm$, $6/mmm$, $-6m2$) crystals [25], which is assumed to be instantaneous. The transverse nonlinear polarization $\tilde{\mathbf{P}}_{\perp}^{\mathrm{NL}}(\mathbf{r},t) = (\tilde{P}_x, \tilde{P}_y)$ can be written by

$$\tilde{P}_x(\mathbf{r},t) = 2\varepsilon_{\mathrm{o}} n_{\mathrm{o}} n_2^{\mathrm{E}} \left[\left(|\tilde{E}_x|^2 + \gamma |\tilde{E}_y|^2 \right) \tilde{E}_x + (1-\gamma) \tilde{E}_x^* \tilde{E}_y^2 \right], \tag{2}$$

$$\tilde{P}_y(\mathbf{r},t) = 2\varepsilon_{\mathrm{o}} n_{\mathrm{o}} n_2^{\mathrm{E}} \left[\left(\gamma |\tilde{E}_x|^2 + |\tilde{E}_y|^2 \right) \tilde{E}_y + (1-\gamma) \tilde{E}_y^* \tilde{E}_x^2 \right], \tag{3}$$

where n_{o} is the ordinary refractive index and n_2^{E} is the nonlinear refractive index. The parameter γ is the ratio of the self-phase modulation (SPM) to the cross-phase modulation (XPM); accordingly, the FWM terms, the last terms in Eqs. (2) and (3), have the coefficients of $1-\gamma$. They are defined by

$$n_{\mathrm{o,e}} = (\varepsilon_{\mathrm{o,e}}/\varepsilon_0)^{1/2}, \tag{4}$$

$$n_2^{\mathrm{E}} n_{\mathrm{o}} \frac{8}{3} = \chi^{(3)}_{xxxx}, \tag{5}$$

$$\gamma n_2^{\mathrm{E}} n_{\mathrm{o}} \frac{8}{3} = \chi^{(3)}_{xxyy} + \chi^{(3)}_{xyxy} = 2\chi^{(3)}_{xxyy}. \tag{6}$$

Here $\chi^{(3)}_{ijkl} = \chi^{(3)}_{ijkl}(-\omega;\omega,\omega,-\omega)$ is a degenerate third-order nonlinear susceptibility tensor, ε_0 is the vacuum permittivity. We consider the beam propagation along the optic axis of a uniaxial crystal. Hence, the axial components $\tilde{E}_z$ and $\tilde{P}_z$ are assumed to remain so small that they can be neglected [24].

With $\tilde{\mathbf{E}}$ and $\tilde{\mathbf{P}}^{\mathrm{NL}}$, the following wave equation is acquired from the Maxwell's equations:

$$-\nabla^2(\tilde{\mathbf{E}}e^{\mathrm{i}kz}) + \nabla[\nabla\cdot(\tilde{\mathbf{E}}e^{\mathrm{i}kz})] + k^2\varepsilon\tilde{\mathbf{E}}e^{\mathrm{i}kz} = -\frac{k^2}{\varepsilon_0}\tilde{\mathbf{P}}^{\mathrm{NL}}e^{\mathrm{i}kz}. \tag{7}$$

Since $\nabla\cdot(\tilde{\mathbf{D}}e^{\mathrm{i}kz}) = 0$,

$$\nabla\cdot(\tilde{\mathbf{E}}e^{\mathrm{i}kz}) = e^{\mathrm{i}kz}\left(1-\frac{\varepsilon_{\mathrm{o}}}{\varepsilon_{\mathrm{e}}}\right)\nabla_\perp\cdot\tilde{\mathbf{E}}_\perp - e^{\mathrm{i}kz}\frac{1}{\varepsilon_{\mathrm{e}}}\nabla_\perp\cdot\tilde{\mathbf{P}}_\perp^{\mathrm{NL}}, \tag{8}$$

where $\tilde{\mathbf{P}}_\perp^{\mathrm{NL}} = (\tilde{P}_x, \tilde{P}_y)$. Here we apply the paraxial approximation to Eq. (7). The paraxial wave equation is

$$2\mathrm{i}k_0 n_{\mathrm{o}}\partial_z\tilde{\mathbf{E}}_\perp + \nabla_\perp^2\tilde{\mathbf{E}}_\perp - \left(1-\frac{\varepsilon_{\mathrm{o}}}{\varepsilon_{\mathrm{e}}}\right)\nabla_\perp(\nabla_\perp\cdot\tilde{\mathbf{E}}_\perp) + \frac{k^2}{\varepsilon_0}\tilde{\mathbf{P}}_\perp^{\mathrm{NL}} = 0. \tag{9}$$

We treat $\partial_z^2\tilde{\mathbf{E}}_\perp$ and $\varepsilon_{\mathrm{e}}^{-1}\nabla_\perp(\nabla_\perp\cdot\tilde{\mathbf{P}}_\perp^{\mathrm{NL}})$ as enough smaller than $(1-\varepsilon_{\mathrm{o}}/\varepsilon_{\mathrm{e}})\nabla_\perp(\nabla_\perp\cdot\tilde{\mathbf{E}}_\perp)$ in this approximation.

To analyze propagation of an axisymmetrically-polarized beam, we introduce the RP component $\tilde{E}_r$ and the AP component $\tilde{E}_\phi$ which are defined by the transverse electric field $\tilde{\mathbf{E}}_\perp$ as,

$$\tilde{\mathbf{E}}_\perp = \begin{pmatrix}\tilde{E}_x\\ \tilde{E}_y\end{pmatrix} = \tilde{E}_r\mathbf{e}_r + \tilde{E}_\phi\mathbf{e}_\phi. \tag{10}$$

#211988 - $15.00 USD Received 13 May 2014; revised 24 Jun 2014; accepted 24 Jun 2014; published 2 Jul 2014

Here, $\mathbf{e}_r$ and $\mathbf{e}_\phi$ are the radial and azimuthal bases, respectively:

$$\mathbf{e}_r = \begin{pmatrix} \cos\phi \\ \sin\phi \end{pmatrix}, \quad \mathbf{e}_\phi = \begin{pmatrix} -\sin\phi \\ \cos\phi \end{pmatrix}, \tag{11}$$

where ϕ is the azimuthal angle $\arctan(y/x)$. Hence, for the axisymmetrically-polarized beam, Eq. (9) is modified to

$$2\mathrm{i}kn_\mathrm{o}\partial_z\tilde{E}_r = -\frac{n_\mathrm{o}^2}{n_\mathrm{e}^2}\left(\partial_r^2 + \frac{1}{r}\partial_r - \frac{1}{r^2}\right)\tilde{E}_r - 2k^2 n_0 n_2^\mathrm{E}\left[\left(|\tilde{E}_r|^2 + \gamma|\tilde{E}_\phi|^2\right)\tilde{E}_r + (1-\gamma)\tilde{E}_\phi^2\tilde{E}_r^*\right], \tag{12}$$

$$2\mathrm{i}kn_\mathrm{o}\partial_z\tilde{E}_\phi = -\left(\partial_r^2 + \frac{1}{r}\partial_r - \frac{1}{r^2}\right)\tilde{E}_\phi - 2k^2 n_0 n_2^\mathrm{E}\left[\left(\gamma|\tilde{E}_r|^2 + |\tilde{E}_\phi|^2\right)\tilde{E}_\phi + (1-\gamma)\tilde{E}_r^2\tilde{E}_\phi^*\right]. \tag{13}$$

In the absence of nonlinearity ($n_2^\mathrm{E} \to 0$), the wave equation can be diagonalized with the RP and AP bases. The RP and AP modes are therefore eigenmodes in the linear propagation; hence these modes independently propagate with different beam divergence [1]. In contrast, the RP and the AP modes are no longer eigenmodes in nonlinear propagation because of the XPM and FWM effects. The XPM and the FWM effects bring phase modulation and energy transfer between the RP and AP modes, respectively.

2.2. Extended Stokes parameters based on cylindrical coordinates

Although the higher-order Stokes parameters [26] can describe an axisymmetrically-polarized state, they are suitable for a uniform, but not for a non-uniform axisymmetrically-polarization state. This indicates that the higher-order Stokes parameters cannot be applied to the propagation of multi-axisymmetrically polarized modes in a uniaxial crystal. In the present subsection, we accordingly introduce the new parameters for describing non-uniform axisymmetrically-polarized beams. These parameters are brought in as a natural extension of the conventional Stokes parameters [27], and are described by integrals of them with respect to the beam cross section and time:

$$\begin{aligned}
S_0^\mathrm{E}(z) &= \iint \left\langle |E_r|^2 + |E_\phi|^2 \right\rangle \mathrm{d}x\mathrm{d}y = \iint S_0 \mathrm{d}x\mathrm{d}y, \\
S_1^\mathrm{E}(z) &= \iint \left\langle |E_r|^2 - |E_\phi|^2 \right\rangle \mathrm{d}x\mathrm{d}y = \iint \left(S_1\cos(2\phi) + S_2\sin(2\phi)\right)\mathrm{d}x\mathrm{d}y, \\
S_2^\mathrm{E}(z) &= \iint \left\langle E_r^* E_\phi + E_r E_\phi^* \right\rangle \mathrm{d}x\mathrm{d}y = \iint \left(-S_1\sin(2\phi) + S_2\cos(2\phi)\right)\mathrm{d}x\mathrm{d}y, \\
S_3^\mathrm{E}(z) &= -\mathrm{i}\iint \left\langle E_r^* E_\phi - E_r E_\phi^* \right\rangle \mathrm{d}x\mathrm{d}y = \iint S_3 \mathrm{d}x\mathrm{d}y
\end{aligned} \tag{14}$$

where the symbol $\langle\cdots\rangle$ and $S_i = S_i(\mathbf{r})$ $(i = 0,1,2,3)$ represent the time average and the conventional Stokes parameters at $\mathbf{r} = (x,y,z)$, respectively. Figure 1 shows typical axisymmetrically polarized modes on the Poincaré sphere for the normalized ESPs ($\tilde{S}_i^\mathrm{E} = S_i^\mathrm{E}/S_0^\mathrm{E}$ $(i = 1-3)$). Axisymmetrically polarized modes can be expressed by the points in the Poincaré sphere for the normalized ESPs. It is noted that, unlike higher-order Stokes parameters [26], the ESPs can define the degree of polarization (DOP) V^E as

$$V^\mathrm{E}(z) = \frac{\left[\left(S_1^\mathrm{E}(z)\right)^2 + \left(S_2^\mathrm{E}(z)\right)^2 + \left(S_3^\mathrm{E}(z)\right)^2\right]^{1/2}}{S_0^\mathrm{E}(z)}. \tag{15}$$

#211988 - $15.00 USD Received 13 May 2014; revised 24 Jun 2014; accepted 24 Jun 2014; published 2 Jul 2014

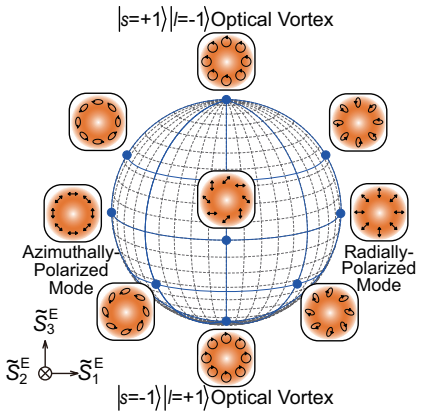

Fig. 1. Poincaré sphere corresponding to the ESPs based on cylindrical coordinates and typical axisymmetrically polarized states (blue points).

The physical meaning of V^{E} is a measure in uniformity of an axisymmetrically polarized state; $V^{\mathrm{E}}=1$, $0<V^{\mathrm{E}}<1$, and $V^{\mathrm{E}}=0$ represent the perfect polarized, partially-polarized and unpolarized states, respectively. In order to exclude the unpolarized state in time domain from V^{E}, we introduce the modified DOP by ESPs,

$$V^{\mathrm{E}}_{\mathrm{space}}(z)=\frac{\left[\left(S_1^{\mathrm{E}}(z)\right)^2+\left(S_2^{\mathrm{E}}(z)\right)^2+\left(S_3^{\mathrm{E}}(z)\right)^2\right]^{1/2}}{\iint S_0(\mathbf{r})V(\mathbf{r})\mathrm{d}x\mathrm{d}y}, \tag{16}$$

where $S_0(\mathbf{r})V(\mathbf{r})=[(S_1(\mathbf{r}))^2+(S_2(\mathbf{r}))^2+(S_3(\mathbf{r}))^2]^{1/2}$ is the amount which is proportional to the time-averaged temporally-perfect-polarized intensity at the position $\mathbf{r}$.

The detail of ESPs, such as expressions of generalized ESPs, the Pancharatnam-Berry phase of the ESPs, will be reported elsewhere.

2.3. ESPs and DOP in linear propagation case

To analyze the nonlinear propagation of axisymmetrically polarized beam, understanding of its linear propagation is a crucial first step. Here we consider the transverse electric field $\tilde{\mathbf{E}}_{\perp}(r,\phi,z\le 0)$ consisting of a RP LG_0^1 and an AP LG_0^1 (LG_p^m is referred as $|l=m\rangle$ Laguerre-Gauss mode with a radial index p) in a uniaxial crystal, which is given by the following equation:

$$\tilde{\mathbf{E}}_{\perp}(r,\phi,z\le 0)=\left(A_r\mathbf{e}_r+A_\phi\mathbf{e}_\phi\right)\frac{r}{w_0\sigma^2(z)}\exp\left(-\frac{r^2}{w_0^2\sigma(z)}\right), \tag{17}$$

where $w_0=(2z_0/k)^{1/2}$ is the waist of the beam in vacuum, $\sigma(z)$ is described by $1-\mathrm{i}[(z-z_{\mathrm{F}})/z_0]$ [21], z_{F} is the focal position in the absence of the crystal, and z_0 is the Rayleigh length. The beam is focused on one of the facets ($z=0$) of c-cut uniaxial crystal ($z\ge 0$).

The solution to Eqs. (12) and (13) in the linear case ($n_2^{\mathrm{E}}\to 0$) inside the uniaxial crystal ($z\ge 0$) is therefore

$$\tilde{\mathbf{E}}_{\perp}(r,\phi,z\ge 0)=A_r\frac{r}{w_0\sigma_r^2(z)}\exp\left(-\frac{r^2}{w_0^2\sigma_r(z)}\right)\mathbf{e}_r+A_\phi\frac{r}{w_0\sigma_\phi^2(z)}\exp\left(-\frac{r^2}{w_0^2\sigma_\phi(z)}\right)\mathbf{e}_\phi, \tag{18}$$

where $\sigma_i(z)=1-\mathrm{i}(z/z_i-z_{\mathrm{F}}/z_0)$ ($i=r,\phi$) with $z_r=(\varepsilon_{\mathrm{e}}^2/\varepsilon_{\mathrm{o}})^{1/2}z_0$ and $z_\phi=(\varepsilon_{\mathrm{o}})^{1/2}z_0$ [19, 21, 22].

#211988 - $15.00 USD Received 13 May 2014; revised 24 Jun 2014; accepted 24 Jun 2014; published 2 Jul 2014

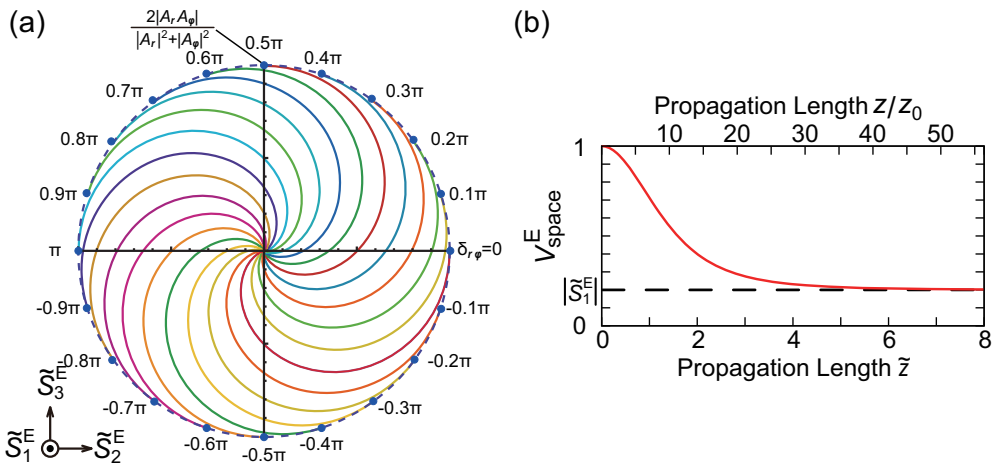

Fig. 2. (a) Trajectories of linear propagations in positive ($\alpha > 0$) uniaxial crystals on a plane of the second and third normalized ESPs. Blue points indicate initial states. (b) DOP $V^{\mathrm{E}}_{\mathrm{space}}$ as a function of the propagation length $\tilde{z} = |\alpha| z/(z_0 n_{\mathrm{o}})$ ($\alpha = 0.237$; calcite at 800 nm) in the linear propagation case [Eq. (22)].

The normalized ESPs and the modified DOP from ESPs are therefore

$$\tilde{S}^{\mathrm{E}}_1(\tilde{z}) = \frac{|A_r|^2 - |A_\phi|^2}{|A_r|^2 + |A_\phi|^2} = \text{const.}, \tag{19}$$

$$\tilde{S}^{\mathrm{E}}_2(\tilde{z}) = 4\left[1 - (\tilde{S}^{\mathrm{E}}_1)^2\right]^{1/2} \cdot \frac{(4-\tilde{z}^2)\cos\delta_{r\phi} + 4\mathrm{sgn}(\alpha)\tilde{z}\sin\delta_{r\phi}}{(4+\tilde{z}^2)^2}, \tag{20}$$

$$\tilde{S}^{\mathrm{E}}_3(\tilde{z}) = 4\left[1 - (\tilde{S}^{\mathrm{E}}_1)^2\right]^{1/2} \cdot \frac{(4-\tilde{z}^2)\sin\delta_{r\phi} - 4\mathrm{sgn}(\alpha)\tilde{z}\cos\delta_{r\phi}}{(4+\tilde{z}^2)^2}, \tag{21}$$

$$V^{\mathrm{E}}_{\mathrm{space}}(\tilde{z}) = \left\{\left[1 - (\tilde{S}^{\mathrm{E}}_1)^2\right]\left(\frac{4}{4+\tilde{z}^2}\right)^2 + (\tilde{S}^{\mathrm{E}}_1)^2\right\}^{1/2}, \tag{22}$$

where $\tilde{z} = |\alpha| z/z_\phi$ is standardized propagation length, $\alpha = (\varepsilon_{\mathrm{e}} - \varepsilon_{\mathrm{o}})/\varepsilon_{\mathrm{e}}$ [20] is birefringence of the uniaxial crystal, sgn is the signum function, and $\delta_{r\phi}$ is the phase difference between A_r and A_ϕ defined by $A_r^* A_\phi = |A_r A_\phi| e^{\mathrm{i}\delta_{r\phi}}$.

From Eq. (19), $\tilde{S}^{\mathrm{E}}_1$ is constant in the linear propagation case where the RP and the AP modes are eigenmodes. Thus, only $\tilde{S}^{\mathrm{E}}_2$ and $\tilde{S}^{\mathrm{E}}_3$ provide the propagation. Figure 2(a) depicts typical trajectories on the $\tilde{S}^{\mathrm{E}}_2$ and $\tilde{S}^{\mathrm{E}}_3$ plane in the linear propagation cases. The trajectories gradually change their curvature with the standardized propagation length $\tilde{z}$; they depend on only initial polarization distribution, being independent of the focus position z_{F}. In particular, the change of $\tilde{S}^{\mathrm{E}}_3$ expresses an interaction between an $|s=-1\rangle|l=+1\rangle$ OV mode and an $|s=+1\rangle|l=-1\rangle$ OV mode, which is called the optical spin-orbit coupling [28] or optical spin-to-orbital angular momentum conversion [29, 30]. The coupling conserves the total angular momentum of photon $j = s + l$. Another highly important feature of the trajectories is that they penetrate the surface of the Poincaré sphere. This is clearly seen from Eq. (22), which shows $V^{\mathrm{E}}_{\mathrm{space}}$ decrease with the propagation distance $\tilde{z}$, as depicted in Fig. 2(b). The decrease in $V^{\mathrm{E}}_{\mathrm{space}}$ is attributed to the decrease in the overlap between the RP and the AP modes with different beam divergences.

#211988 - $15.00 USD Received 13 May 2014; revised 24 Jun 2014; accepted 24 Jun 2014; published 2 Jul 2014

3. Experiment

3.1. Experimental setup

Figure 3(a) shows the experimental setup for the nonlinear propagation of axisymmetrically-polarized pulses. The light source used is a Ti:sapphire laser amplifier (center wavelength 800 nm, pulse duration ~ 25 fs, and repetition rate 1 kHz) . A pulse with a duration of $\sim$120 fs after a 800 ± 5 nm bandpass filter (BP), is converted to an $|s=+1\rangle|l=-1\rangle$ OV pulse by passing through a quarter-wave plate (QWP1) and a spiral phase plate (SPP). This $|s=+1\rangle|l=-1\rangle$ OV pulse is focused on one of the surfaces of a 2 mm- or 5 mm-thick *c*-cut calcite crystal (CR) by a convex lens L1. We refer to the surface ($z=0$) and the other surface ($z=L$) as the input surface and the output surface, respectively. Since the NA and Rayleigh length of the input beam are respectively $\sim$0.02 and $z_0 = 0.5$ mm, $|\tilde{E}_z|$ is quite small enough to be neglected [13]. After propagating along the optic axis of the crystal, the beam is collimated by another convex lens L2. By using a quarter-wave plate (QWP2) or half-wave plate (HWP), linearly *x*-, *y*-, $+45^\circ$-, -45°-polarized, and left- and right-circularly polarized beams [Fig. 3(b) left], after passing through a polarizing beam splitter (PBS), are guided to a charge-coupled-devise (CCD) camera and their intensity profiles are recorded so that the ESPs can be derived from the conventional Stokes parameters $(S_1(x,y), S_2(x,y), S_3(x,y))$ [31] by using Eqs. (14) [Fig. 3(b) middle and right]. To enhance the properties of the nonlinear propagation, we move the focal position z_F (in the absence of CR) [Fig. 3(a)]. This enables us to control the beam overlapping, thereby the amount of the energy transfer between a RP mode and an AP mode, which will be mentioned in sections 3.2 and 4. We here define two typical focal position $z^\mathrm{A}_\mathrm{F,out}$ and $z^\mathrm{R}_\mathrm{F,out}$, where the focus of the AP mode is at output facet and that of the RP mode is at output facet, respectively [Fig. 3(c)].

3.2. Experimental results

To analyze the nonlinear propagation of $|s=+1\rangle|l=-1\rangle$ OV pulses in a uniaxial crystal, we derive the changes of $\tilde{S}^\mathrm{E}_1$ and $V^\mathrm{E}_\mathrm{space}$ from the linear values

$$\Delta\tilde{S}^\mathrm{E}_1 = \tilde{S}^\mathrm{E}_1 - \tilde{S}^\mathrm{E,Linear}_1, \tag{23}$$

$$\Delta V^\mathrm{E}_\mathrm{space} = V^\mathrm{E}_\mathrm{space} - V^\mathrm{E,Linear}_\mathrm{space}. \tag{24}$$

We can investigate the FWM effect giving energy transfer between the RP and AP modes, through $\Delta\tilde{S}^\mathrm{E}_1$. In addition, the SPM and XPM effects can be analyzed through $\Delta V^\mathrm{E}_\mathrm{space}$ since the phase modulation effects involving beam-divergence change modify beam overlap of these modes.

The experimentally-obtained ΔS^E_1 and $\Delta V^\mathrm{E}_\mathrm{space}$ are respectively plotted in Figs. 4(a), 4(b) and 4(c), 4(d), as functions of the focal position z_F. The cyan, orange and green bars in Fig. 4 correspond to the focus positions where the focus of the input beam is at the input facet of crystal ($z_\mathrm{F}=0$), that of the AP mode is at the output facet of crystal ($z_\mathrm{F} = z^\mathrm{A}_\mathrm{F,out}$) and that of the RP mode is at the output facet of crystal ($z_\mathrm{F} = z^\mathrm{R}_\mathrm{F,out}$), respectively [Fig. 3(c)]. From Eq. (18), the relationships between $z^\mathrm{A,R}_\mathrm{F,out}$ and crystal length L are

$$n_\mathrm{o} z^\mathrm{A}_\mathrm{F,out} = 1.65 z^\mathrm{A}_\mathrm{F,out} = L, \qquad \frac{n^2_\mathrm{e}}{n_\mathrm{o}} z^\mathrm{R}_\mathrm{F,out} = 1.33 z^\mathrm{R}_\mathrm{F,out} = L, \tag{25}$$

for calcite crystals at 800 nm [32]. Intensity dependent peaks of ΔS^E_1 appear at $z_\mathrm{F} \simeq 1$ mm in both the 2 mm- and 5 mm-thick calcite [Figs. 4(a) and 4(b)]. The maximum values $\Delta S^\mathrm{E,max}_1$ at these peaks are proportional to the input pulse energy. The positive value of $\Delta\tilde{S}^\mathrm{E}_1$ reflects the

#211988 - $15.00 USD Received 13 May 2014; revised 24 Jun 2014; accepted 24 Jun 2014; published 2 Jul 2014

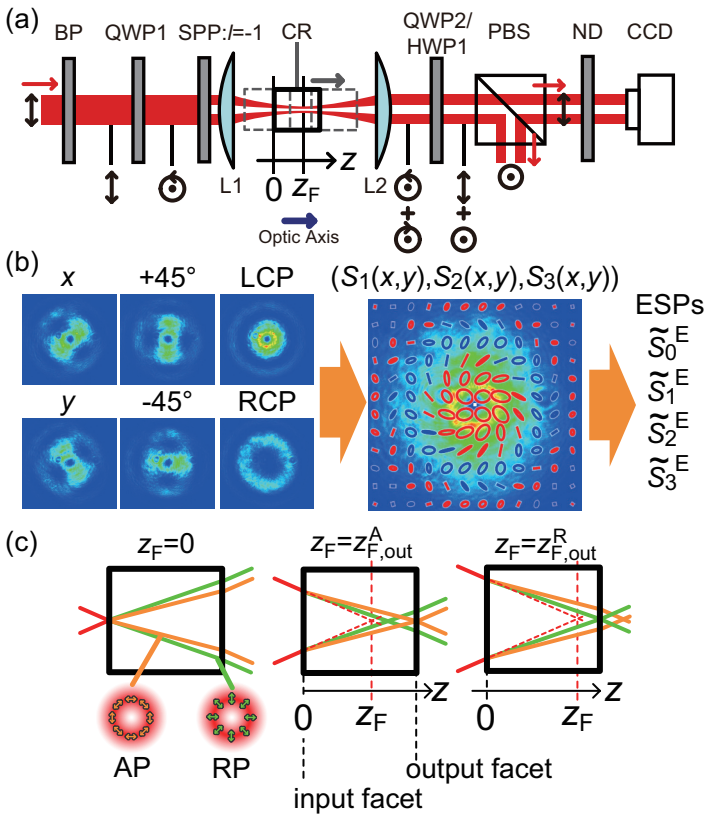

Fig. 3. (a) Setup for nonlinear propagation of axisymmetrically polarized pulses. BP, a bandpass filter; QWP1,2, quarter-wave plates; HWP, a half-wave plate; SPP, a spiral phase plate ($l=-1$); L1,2, convex lenses; CR, a nonlinear crystal (a 2 mm- or 5 mm-thick c-cut calcite crystal); PBS, a polarizing beam splitter; ND, a neutral density filter. z_F is the relative position between the input surface of CR and the focal point of the input beam (without CR). (b) The flow chart to obtain the ESPs. x, y, $+45^\circ$ and -45° represent intensity distributions of linearly x-, y-, $+45^\circ$-, -45°-polarized components, respectively. LCP and RCP represent intensity distributions of LCP and RCP components, respectively. Spatial-dependent, conventional Stokes parameters $(S_1(x,y),S_2(x,y),S_3(x,y))$ obtained from these six intensity profiles provide ESPs. (c) Schematic definitions of z_F, $z^A_{F,out}$ and $z^R_{F,out}$. The red, green and orange lines stand for the beam paths of $|s=+1\rangle|l=-1\rangle$ OV, the RP and AP modes, respectively.

energy transfer from the AP mode to the RP mode. The energy transfer occurs in the region of $-1 \lesssim z_F \lesssim 2$ mm for the 2 mm calcite and $-1 \lesssim z_F \lesssim 3$ mm for the 5 mm-thick calcite. In Figs. 4(c) and 4(d), positive and negative peaks of ΔV^E_{space} appear at $z_F = 0$ mm and $z_F = z^A_{F,out}$, respectively. The heights of these peaks are also proportional to the energy of the input pulses. These experimental results will be analyzed and compared with the simulation results in section 4.

4. Discussion

Since the difference of the group delay between the AP and the RP pulses is estimated to be about 5 fs after propagation in 5 mm-thick calcite, the temporal delay between these pulses can

#211988 - $15.00 USD Received 13 May 2014; revised 24 Jun 2014; accepted 24 Jun 2014; published 2 Jul 2014

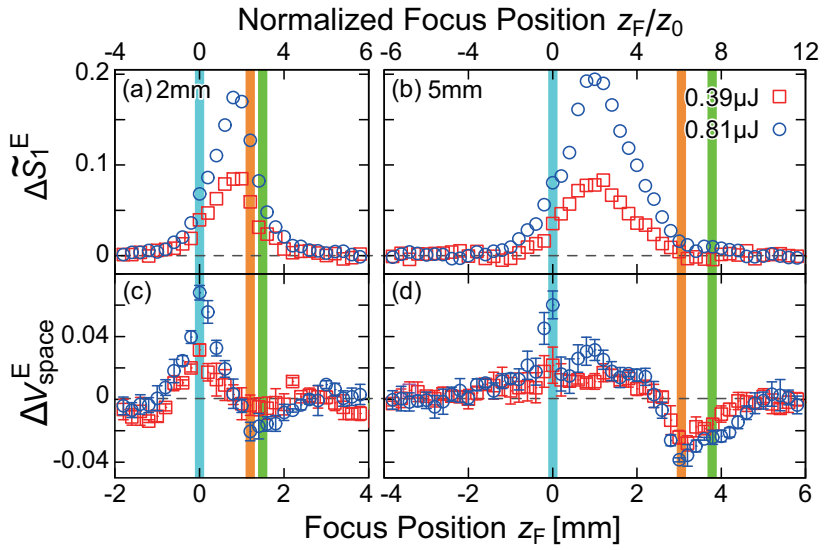

Fig. 4. Experimental results. $\Delta\tilde{S}_1^{\mathrm{E}}$ after the nonlinear propagation of (a) 2mm($\simeq 4z_0$) and (b) 5mm($\simeq 10z_0$) *c*-cut calcite. $\Delta V_{\mathrm{space}}^{\mathrm{E}}$ after the nonlinear propagation of (c) 2mm and (d) 5mm *c*-cut calcite. Each graph has results for two pulse energy: 0.39 μJ and 0.81 μJ. The cyan bars represent the focus position where the focus of the input beam is at the input facet ($z_{\mathrm{F}} = 0$). The orange and green bars correspond to the focus positions z_{F} where the foci of the AP and the RP modes are at the output facet, respectively.

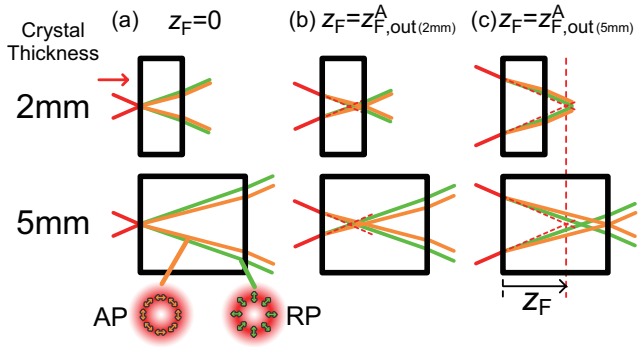

Fig. 5. Trajectories for $|s=+1\rangle|l=-1\rangle$ OV (red line), RP mode (green line) and AP mode (orange line) inputs. (a) The focus of input beam corresponds to the input facet of the crystals ($z_{\mathrm{F}} = 0\,$mm). The focus of the AP mode corresponds to the output facet of (b) 2 mm-thick CR ($z_{\mathrm{F}} \sim 1.2\,$mm) and (c) that of 5 mm-thick CR ($z_{\mathrm{F}} \sim 3.0\,$mm).

be neglected in our experiments. Variations of $\Delta\tilde{S}_1^{\mathrm{E}}$ and $\Delta V_{\mathrm{space}}^{\mathrm{E}}$ as functions of z_{F} in Fig. 4 are therefore ascribed to a change in spatial overlap or relative focus positions between the AP and the RP pulses.

Figure 5 schematically describes the focus positions of the AP and the RP pulses with various z_{F} (the focal position (in the absence of the crystal) relative to the input crystal surface). In the region of $0 \lesssim z_{\mathrm{F}} \lesssim z_{\mathrm{F,out}}^{\mathrm{A}}$, the RP and AP modes considerably overlap each other. The relative distance between the foci of the AP and the RP pulses increases with an increase in z_{F} owing to the crystal anisotropy. The spatial overlap therefore decreases with an increase in z_{F}.

#211988 - $15.00 USD Received 13 May 2014; revised 24 Jun 2014; accepted 24 Jun 2014; published 2 Jul 2014

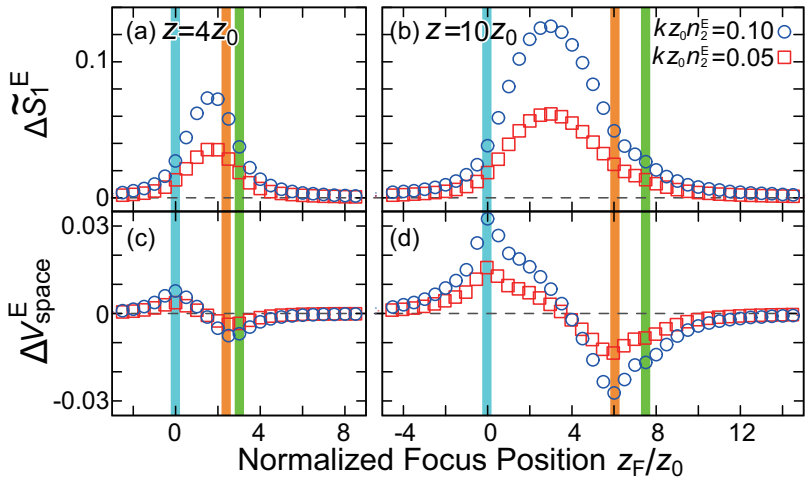

Fig. 6. Simulation results for focus position dependence of $\Delta\tilde{S}_1^{\mathrm{E}}$ and $\Delta V_{\mathrm{space}}^{\mathrm{E}}$ at two standardized crystal lengths. (a) and (c) $z = 4z_0$; (b) and (d) $z = 10z_0$ ($\gamma = 2/3$). The cyan bars represent the focus position where the input beam is at the input facet ($z_{\mathrm{F}} = 0$). The orange and green bars correspond to the focus positions z_{F} where the foci of the AP and the RP modes are at the output facet, respectively.

To make sure that the spatial overlap mainly gives the variations of $\Delta\tilde{S}_1^{\mathrm{E}}$ and $\Delta V_{\mathrm{space}}^{\mathrm{E}}$, we perform simulations, for simplicity, on the assumption that the input transverse electric field $\tilde{\mathbf{E}}_{\perp}(r,\phi,z\leq 0)$ is described by Eq. (17) (See Appendix for the detail of the simulations). Figures 6(a)–6(d) show $\Delta\tilde{S}_1^{\mathrm{E}}$ and $\Delta V_{\mathrm{space}}^{\mathrm{E}}$ as a function of the focal position z_{F} at propagation distances of $z = 4z_0\,(\sim 2\mathrm{mm})$ and $z = 10z_0\,(\sim 5\mathrm{mm})$. The experimental results (Fig. 4) agree with these simulation results.

The experimental and simulation results show that $\Delta\tilde{S}_1^{\mathrm{E}}$ has positive peaks and its peak heights increase with increasing pulse energy in the region of $0 \lesssim z_{\mathrm{F}} \lesssim z_{\mathrm{F,out}}^{\mathrm{A}}$, where the RP and AP modes well overlap each other. The observed pulse energy dependence of $\Delta\tilde{S}_1^{\mathrm{E}}$ indicates the energy transfer from an AP pulse to a RP pulse in the terms of the FWM effect, which is well explained by Eqs. (12) and (13). In these wave equations only the terms $(1-\gamma)\tilde{E}_{\phi}^2\tilde{E}_r^*$ and $(1-\gamma)\tilde{E}_r^2\tilde{E}_{\phi}^*$ give energy transfer between the AP and RP pulses, depending on the pulse energy and the spatial overlap between them.

Nonlinear DOP change $\Delta V_{\mathrm{space}}^{\mathrm{E}}$ mainly reflects the SPM and FWM effects. Equation (22) shows that $V_{\mathrm{space}}^{\mathrm{E}}$ depends on the propagation length $\tilde{z} = |\alpha|z/(z_0 n_{\mathrm{o}})$; $V_{\mathrm{space}}^{\mathrm{E}}$ monotonically decrease with $\tilde{z}$, as shown in Fig. 2(b). The SPM and FWM effects induce wide beam divergence in the region of $z_{\mathrm{F}} \gtrsim 0$ or narrow beam divergence in the region of $z_{\mathrm{F}} \lesssim 0$. This induced wide or narrow divergence makes the effective optical propagation length long or short, giving $\Delta V_{\mathrm{space}}^{\mathrm{E}} < 0$ or $\Delta V_{\mathrm{space}}^{\mathrm{E}} > 0$, respectively, from the monotonical decreasing of $V_{\mathrm{space}}^{\mathrm{E}}$ on $\tilde{z}$. The negative peaks at $z_{\mathrm{F}} = z_{\mathrm{F,out}}^{\mathrm{A}}$ (orange lines) in Figs. 4(c) and 4(d), and Figs. 6(c) and 6(d) are also explained by the SPM and XPM effects. They make the focal length shorter at $z_{\mathrm{F}} = z_{\mathrm{F,out}}^{\mathrm{A}}$, thereby giving the longer effective optical propagation length and the decrease in $\Delta V_{\mathrm{space}}^{\mathrm{E}}$.

In the experiment, the pulse contains not only a LG_0^{-1} mode but also $\mathrm{LG}_{p\neq 0}^{-1}$ modes. The higher-p LG mode undergoes the larger Gouy phase shift [33]. We have carried out numerical simulations in the case where $\tilde{\mathbf{E}}_{\perp}(r,\phi,z\leq 0)$ is expressed by the mixed mode with $p = 0, 1$ and 2, whose results resembling the experimental results somewhat better than those with an only

#211988 - $15.00 USD Received 13 May 2014; revised 24 Jun 2014; accepted 24 Jun 2014; published 2 Jul 2014

$p = 0$ mode. This implies that $p \neq 0$ submodes contribute the nonlinear propagation.

5. Conclusion

In conclusion, we have experimentally and theoretically investigated nonlinear propagation of axisymmetrically-polarized ultrashort optical pulses along the optic axis in a uniaxial crystal under the condition that a circularly-polarized optical-vortex pulse is focused into the crystal. The energy transfer between an AP pulse and a RP pulse through FWM effect was observed. To analyze the experimental results, we have derived a general paraxial equation with a third-order nonlinearity for axisymmetrically-polarized pulses in a uniaxial crystal and have newly introduced the extended Stokes parameters, ESPs, based on cylindrical coordinates. The simulation results providing the ESPs, well explain our experimental results. One of the distinct results is the energy transfer between the axisymmetrically polarized modes, which is attributed to the FWM effect. The change of $\Delta\tilde{S}_1^{\mathrm{E}}$, the energy transfer from the AP to the RP pulses can be utilized as an all-optical ultrafast switch for vector-vortex-mode-division multiplexing in optical communications. We can control the transfer direction by using a positive uniaxial crystal instead of a negative crystal (See Appendix). This phenomenon occurs in any crystals which have non-diagonal $\chi^{(3)}$ nonlinearity and uniaxial refractive indices in transparent wavelength region (for calcite, its transparent region is from 0.24 to 2.2 μm [32]). However, in case that the pulse duration is shorter than ~ 100 fs for a wavelength of ~ 800 nm, the correction of the slowly-varying envelope approximation (or higher-order approximation) is required. Furthermore, the DOP defined from the ESPs is measured as a function of the focal position and is clarified to be affected by the SPM and XPM, which make the effective propagation length long or short. Thus, the nonlinear interaction in a uniaxial crystal modifies the axisymmetrically-dependent polarization distribution and has potential to obtain an axisymmetrically-full Poincaré state [34].

Appendix

In our simulation in section 4, we employ the Runge-Kutta and pseudo-spectrum methods for z- and r-differentiations, respectively. Since wave equations, Eqs. (12) and (13), have off-diagonal components, the split-step Fourier method cannot be used here [24]. With $\tilde{z} = z/z_0$ and $\tilde{r} = r/w_0$, we normalize the wave equations as follows:

$$\partial_{\tilde{z}}\tilde{E}_r = \mathrm{i}\left\{\frac{n_{\mathrm{o}}}{4n_{\mathrm{e}}^2}\left(\partial_{\tilde{r}}^2 + \frac{1}{\tilde{r}}\partial_{\tilde{r}} - \frac{1}{\tilde{r}^2}\right)\tilde{E}_r + kz_0 n_2^{\mathrm{E}}\left[(|\tilde{E}_r|^2 + \gamma|\tilde{E}_\phi|^2)\tilde{E}_r + (1-\gamma)\tilde{E}_\phi^2\tilde{E}_r^*\right]\right\}, \quad (26)$$

$$\partial_{\tilde{z}}\tilde{E}_\phi = \mathrm{i}\left\{\frac{1}{4n_{\mathrm{o}}}\left(\partial_{\tilde{r}}^2 + \frac{1}{\tilde{r}}\partial_{\tilde{r}} - \frac{1}{\tilde{r}^2}\right)\tilde{E}_\phi + kz_0 n_2^{\mathrm{E}}\left[(\gamma|\tilde{E}_r|^2 + |\tilde{E}_\phi|^2)\tilde{E}_\phi + (1-\gamma)\tilde{E}_r^2\tilde{E}_\phi^*\right]\right\}. \quad (27)$$

Equations (26) and (27) (or (12) and (13)) are invariance under a permutation such that $n_{\mathrm{o}} \to n_{\mathrm{e}}^2/n_{\mathrm{o}}$, $\tilde{E}_r \to \tilde{E}_\phi$ and $\tilde{E}_\phi \to \tilde{E}_r$. This permutation gives the birefringence-sign inversion and a swap of the electric field components, $\tilde{E}_r$ and $\tilde{E}_\phi$. The energy transfer direction is therefore determined by the sign of the anisotropy of the crystal. Hence, we can control or switch the transfer direction by using a positive uniaxial crystal instead of a negative crystal.

In the experiment, we used a spiral phase plate to generate $|s=+1\rangle|l=-1\rangle$ OV pulses from $|s=+1\rangle|l=0\rangle$ Gaussian pulses. The generated beam $\tilde{E}^{(\mathrm{gen})}(\mathbf{e}_r + i\mathbf{e}_\phi)$ is consequently not an LG_0^{-1} beam but is generally expressed by a superposition of LG_p^{-1} beams with all radial indices p:

$$\tilde{E}^{(\mathrm{gen})} = A^{(\mathrm{gen})}\sum_{p=0}^{\infty}\frac{\pi^{1/2}(2p-1)!!}{2(p+1)(2p)!!}u_{-1p}, \quad (28)$$

#211988 - $15.00 USD Received 13 May 2014; revised 24 Jun 2014; accepted 24 Jun 2014; published 2 Jul 2014

where $A^{(\mathrm{gen})}$ is a constant coefficient. Equation (28) is obtained by using Laguerre series expansion [35]. The function u_{mp} denotes the LG_p^m mode given by [33]

$$u_{mp} = \left(\frac{\sqrt{2}r}{w_0|\sigma(z)|}\right)^{|m|} L_p^{|m|}\left(\frac{2r^2}{w_0^2|\sigma(z)|^2}\right)\frac{1}{|\sigma(z)|}\exp\left(-\frac{r^2}{w_0^2\sigma(z)} + \mathrm{i}m\phi - \mathrm{i}\Psi_{\mathrm{G}}(z)\right), \quad (29)$$

where $L_p^{|m|}$ is the generalized Laguerre polynomial and $\Psi_{\mathrm{G}}(z)$ is the Gouy phase defined by

$$\Psi_{\mathrm{G}}(z) = (2p + |m| + 1)\arctan(z/z_0). \quad (30)$$

The simulations in section 4 are conducted on the assumption that the input transverse electric field $\tilde{\mathbf{E}}_\perp(r,\phi,z \le 0)$ is described by Eq. (17) (the dominant mode ($p = 0$) in Eq. (28)). We assume that the absolute value of the fundamental mode is normalized so that the maximum of the absolute value of the input beam at its focus is unity ($A_r = -\mathrm{i}A_\phi = [\exp(1)/2]^{1/2}$ in Eq. (17)). Calculations were done under the condition that $kz_0 n_2^{\mathrm{E}} = 0.1$, $\gamma = 2/3$, the wavelength of OV is 800 nm, and a calcite ($n_{\mathrm{o}} = 1.64, n_{\mathrm{e}} = 1.48$ [32]) is used as a nonlinear crystal.

Acknowledgment

This work was partially supported by Grant-in-Aid for Scientific Research (B) (No. 23360024, 2011-2014) from Japan Society for the Promotion of Science (JSPS).